

Second-harmonic near-field imaging of ferroelectric domain structure of YMnO₃

Catalin C. Neacsu,¹ Bas B. van Aken,² Manfred Fiebig,² and Markus B. Raschke¹

¹*Department of Chemistry, University of Washington, Seattle, Washington 98195, USA*

²*HISKP, Universität Bonn, Nussallee 14-16, D-53115 Bonn, Germany*

(Received 4 February 2009; published 23 March 2009)

Near-field tip-enhanced and symmetry-selective nonlinear light scattering is demonstrated for imaging nanoscopic ferroelectric order. The surface topology of antiparallel ferroelectric domains in multiferroic YMnO₃ is spatially resolved by second-harmonic generation (SHG). Optical phase contrast is obtained by interference between the local near-field SHG and a self-homodyne far-field reference SHG field. Ferroelectric domains anisotropically elongated along the hexagonal crystallographic axis were found, with typical dimensions of $\sim 1000 \times 200$ nm². The irregular domain shapes seem to contrast the behavior of ordinary ferroelectrics. Relying on symmetry properties only, SHG scattering-type scanning near-field optical microscopy can be extended to probe any ferroic order.

DOI: 10.1103/PhysRevB.79.100107

PACS number(s): 77.80.Dj, 42.65.Ky, 68.37.Uv, 78.20.-e

Ferroelectric materials are characterized by the spontaneous formation of local electric polarization in the form of domains. Controlling their spatial arrangement is the foundation of the ferroelectric random access memory¹ and of several electro-optical^{2,3} and nanomechanical device applications.⁴ A particular need to understand the ferroelectric domain behavior has emerged recently when it was discovered that in multiferroics the ferroelectric state can couple rigidly to a magnetically ordered state—either intrinsically⁵ or via a ferroelectric substrate with tunable lattice constant.⁶ In this regard YMnO₃ has attracted much interest as an intrinsic multiferroic.

With the virtue of its symmetry selectivity optical second-harmonic (SH) generation (SHG) is particularly attractive for probing the ferroelectric state. The second-order nonlinear optical polarization is given by $P_i(2\omega) = \epsilon_0 \hat{\chi}_{ijk}^{(2)} E_j(\omega) E_k(\omega)$ with electric fields $E_{j,k}(\omega)$ of the incident light waves and $(i, j, k) \in (x, y, z)$. With the second-order susceptibility tensor $\hat{\chi}_{ijk}^{(2)} \neq 0$ for noncentrosymmetric systems only, SHG couples directly to the symmetry-breaking ferroelectric order parameter.⁷ This led to the successful implementation of far-field (FF) SH microscopy for the investigation of ferroelectrics.⁸⁻¹⁰ With technologically relevant ferroelectric domains being of nanoscopic dimensions, the use of aperture-based scanning near-field (NF) optical microscopy (SNOM) has been explored to obtain subdiffraction spatial resolution.¹¹⁻¹⁵ However, restrictions in terms of polarization selection of $P_i(2\omega)$, $E_i(\omega)$, and $E_j(\omega)$, as imposed by the glass-fiber probes,¹⁶ as well as of k -vector conservation due to the laws of nonlinear refraction and/or reflection at interfaces,¹⁷ restrain the applicability of these techniques to a limited range of crystal symmetries.

Here, we show that scattering-type scanning near-field optical microscopy (*s*-SNOM) SHG allows for unrestricted probing of ferroelectric order. *s*-SNOM has previously been applied in special cases for ferroelectric domain imaging by probing the linear electro-optic coefficient^{18,19} and SHG in transmission geometry.²⁰ We provide a general treatment of SHG *s*-SNOM for ferroelectric structure imaging. As sensitive local probes for the near-field SHG, metallic scanning tips can project the individual vector field components of the individual polarizations $P_i(2\omega)$ into the far field by SH scattering. This together with the independent selection of

k -vector and polarization directions of both pump and SH fields enables specific selection of individual susceptibility tensor components $\hat{\chi}_{ijk}^{(2)}$ sensitive to the ferroelectric polarization and to any ferroic order in general. Imaging with nanometer spatial resolution is achieved taking advantage of the near-field enhancement provided by the tip apex.²¹

We resolve the surface topology of nanoscale ferroelectric antiparallel domains in YMnO₃. In contrast to the well-established *pd*-hybridization-type ferroelectricity found in classical ferroelectrics such as BaTiO₃ and PbTiO₃²² with the Ti⁴⁺ cation being in the d^0 state, the coexistence of magnetic and ferroelectric orders in general is only possible for occupied d shells, i.e., d^n , $n > 0$.²³ Ferroelectricity in multiferroics is of a yet poorly understood geometric/electrostatic type.^{24,25} The ferroelectricity in YMnO₃ arises from a buckling of the MnO₅ polyhedra and concerted Y³⁺ ion displacement.²⁶ This results in a polarization of $5.5 \mu\text{C}/\text{cm}^2$ directed along $\vec{P}_s = (0, 0, \pm P_z)$.²⁷ Using YMnO₃ as model compound exhibits the general nature of the approach of scattering SH near-field domain imaging. The method is independent of the type of ferroelectricity and the microscopic mechanism leading to the ferroelectric state, because it is only based on symmetry. With \vec{z} as hexagonal axis the point symmetry is reduced from centrosymmetric $6/mmm$ to noncentrosymmetric $6mm$ by the paraelectric to ferroelectric phase transition. The ferroelectric order parameter P is reflected in the $\hat{\chi}^{(2)}$ tensor symmetry as $\hat{\chi}^{(2)}(\pm P) = \pm P \hat{\chi}_0^{(2)}$. Thus opposite domains with $\pm P$ lead to a SH polarization of identical amplitude but with a 180° relative phase. Imaging contrast between these antiparallel domains thus requires phase-sensitive SHG detection.^{28,29} This is achieved here by the interference of the tip-scattered near-field SH polarization of neighboring domains with a tip-scattered far-field signal from the sample serving as a local self-homodyne phase reference.

The experiments are performed on a single-crystalline *x*-cut YMnO₃ sample grown by the floating-zone technique. With ferroelectrics known to form surface-pinned cap layers,³⁰ sample polishing insures that the observed ferroelectric domain structure reflects the unperturbed bulk. The ferroelectric phase with its $6mm$ symmetry corresponds to a tensor $\chi^{(2)}$ that has only three independent elements $\chi_{xxz}^{(2)}$

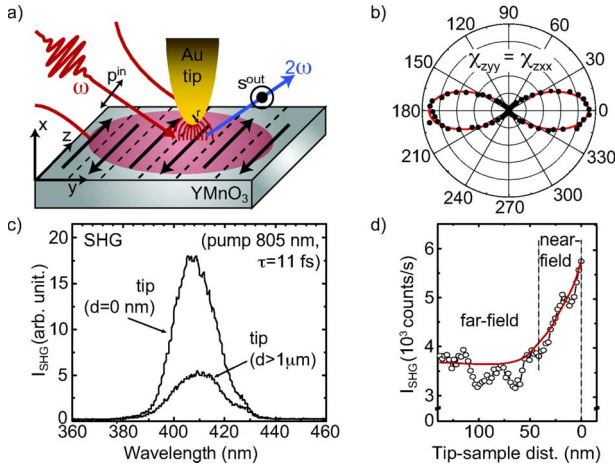


FIG. 1. (Color online) (a) Tip-scattering near-field SHG imaging with self-homodyne detection of ferroelectric order in YMnO₃. (b) Far-field SHG anisotropy measurement in transmission is used for sample orientation. (c) Spectrally resolved near- and far-field SHG signals. (d) Dependence of total SHG signal on tip-sample distance with the solid line as guide for the eyes.

$=\chi_{zxx}^{(2)}=\chi_{yyz}^{(2)}=\chi_{yzy}^{(2)}$, $\chi_{zxx}^{(2)}=\chi_{zyy}^{(2)}$, and $\chi_{zzz}^{(2)}$. Here, only $\chi_{zxx}^{(2)}$ needs to be considered since it is >10 times larger than the other components in the visible spectral range.³¹

The experimental setup is based on a home-built shear-force atomic force microscope (AFM). Electrochemically etched gold tips with apex radii of 10–25 nm are used as optical probes.³² The sample is scanned to ensure constant illumination conditions of the tip apex. A mode-locked Ti:sapphire oscillator (Femtolasers Inc., with pulse duration $\tau \approx 11$ fs, center wavelength of 810 nm, and repetition rate of 78 MHz) provides the pump radiation for SHG. In an epi-illumination and -detection geometry the probe tip is illuminated using a long working distance microscope objective (numerical aperture =0.35, and working distance =20.5 mm) with angle of incidence $\theta \approx 70^\circ$ with respect to the tip axis [Fig. 1(a)]. To achieve ultrashort pulse duration at the tip as desired for efficient SH generation a chirped mirror dispersion precompensator (Femtolasers Inc.) results in $\tau \sim 13$ fs pulse duration in the focal plane of objective. With a focus diameter of $\sim 2.5 \mu\text{m}$ for the incident pump light, the maximum power of 20 mW (0.13 nJ pulse energy) employed corresponds to a power density of 0.2 MW/cm². The incident and detected polarizations can be controlled, with s and p defined perpendicular and parallel with respect to the plane of incidence formed by incident/emitted wave vector and tip axis. The tip-scattered SHG signal is recorded simultaneously with the topography of the sample. The SHG light passes a polarizer, is spectrally filtered, and is detected alternatively by an imaging spectrograph with liquid-nitrogen-cooled charge-coupled device or an avalanche photodiode with photon counting electronics.

Tip-enhanced excitation of the desired $\chi_{zxx}^{(2)}$ component is achieved by choosing the xy plane of the sample as plane of incidence as shown in Fig. 1(a). Light polarized in this plane (index p) has x - and y -polarized contributions while light polarized perpendicular to this plane (index s) is z polarized. Therefore, $\chi_{zxx}^{(2)}$ is selected in the $p_{in}s_{out}$ configuration. The

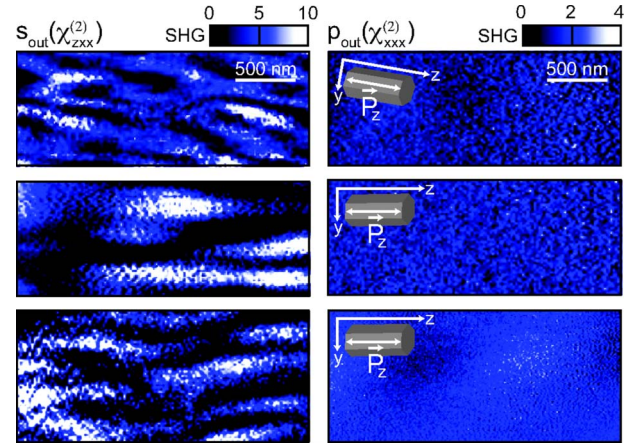


FIG. 2. (Color online) Self-homodyne SHG interferometric s -SNOM imaging of ferroelectric domains of YMnO₃ (100) for $p_{in}s_{out}$ (left panels) and $p_{in}p_{out}$ (right panels) polarization combinations of three different regions of the sample. In the first panel the z axis is rotated about 10° with respect to the horizontal scan direction. Contrast is obtained for $p_{in}s_{out}$ probing the $\chi_{zxx}^{(2)}$ tensor component specific to the ferroelectric order. No significant contrast is obtained in $p_{in}p_{out}$ with $\chi_{xxx}^{(2)}=0$ for YMnO₃.

crystallographic y and z directions of the x -cut sample are identified by independent far-field rotational SHG anisotropy measurement [Fig. 1(b)] carried out under normal incidence in transmission. Here, $\vec{E}(\omega)$ and the component of $\vec{P}(2\omega)$ oriented perpendicular to $\vec{E}(\omega)$ are rotated simultaneously. This leads to a SHG intensity variation that can be fitted using $I(2\omega) \propto \cos^6 \alpha$ with $\alpha = \angle(\vec{E}(\omega), \vec{y})$, thus identifying the crystallographic directions.³¹

Figure 1(c) shows the spectrally resolved SHG intensity I_{SHG} for the configuration $p_{in}s_{out}$ for tip-sample distances $d = 0$ nm (near field) and $d > 1 \mu\text{m}$ (far field), respectively. Measurements of $I_{SHG}(d)$ as shown in Fig. 1(d) allow the distinction of these two regions of interest. In the region $d > 30$ nm the SHG signal is dominated by the tip-scattered far-field SH response of the sample. This far-field SH contribution varies laterally slowly with distance on a length scale of several μm , essentially determined by the focus size. For $d < 30$ nm the spatial variation of the local tip-enhanced SH response is correlated with the tip apex radius of ~ 20 nm. The explicit dependence of $I_{SHG}(d)$ in this range is determined by the interference between the tip-scattered near-field SH response and the far-field SH signal of YMnO₃, in addition to small SH contributions generated by the tip itself.

Figure 2 shows the tip-scattered SHG near-field image of YMnO₃ for the $p_{in}s_{out}$ (left panels) in comparison to the $p_{in}p_{out}$ (right panels) polarization configurations for three sample regions representative for the different ranges of domain sizes and patterns observed. In the first measurement the z axis of the sample has been rotated about 10° with respect to the scanning direction to confirm the near-field domain imaging process. The scan size is $2.56 \times 1 \mu\text{m}^2$ acquired for 128×100 pixels with a signal integration time of 30 ms/pixel. With the s -polarized SHG selectively probing the ferroelectric $\chi_{zxx}^{(2)}$ tensor component the optical contrast observed can then be attributed to the intrinsic ferroelectric

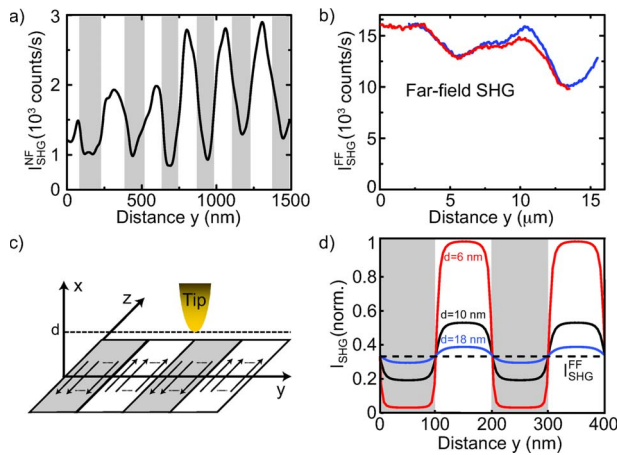


FIG. 3. (Color online) (a) Cross-sectional profile of near-field SH data with domain assignment applying the discrete dipole model. (b) Far-field SHG response of constant phase exhibits small intensity variations on a length scale given by the laser focus only. (c) Schematics of the discrete dipole model for domain wall assignment with 1-nm-spaced dipoles oriented along the z axis representing a $P_z^{(2)}(2\omega)$ density for antiparallel domains. (d) Calculated resulting tip-scattered SHG intensity and contrast for three different tip-sample separations d . The dashed line represents the far-field signal intensity.

domain structure of the YMnO_3 sample. In contrast, $\chi_{xxx}^{(2)}$ and $\chi_{xyy}^{(2)}$ are zero in YMnO_3 , so that for $p_{\text{in}}p_{\text{out}}$ no significant contrast is observed. The SHG signal in this case arises mainly from the tip apex itself which generates surface SH due to the broken symmetry in its axial direction (∞mm) for $p_{\text{in}}p_{\text{out}}$. In the $p_{\text{in}}s_{\text{out}}$ configuration the tip emits only weak SHG arising from nonlocal higher-order bulk contributions.³³

The image contrast arises from the interference between two signal contributions: (i) the spatially confined tip-enhanced NF SHG signal which exhibits a 180° phase change whenever a domain wall is crossed and (ii) the FF SHG light emitted from the ensemble of domains located within the incident laser focus and backscattered by the tip. Here, even for a homogeneous distribution of domains with $\pm P_z$ the far-field signal does not fully cancel by interference from opposite domains but results in a phase-stable (ϕ_{FF}) reference wave. This is because phase retardation and the lateral and vertical spatial domain distributions excited within the laser focus affect the interference process.³⁴ The total SHG s -SNOM intensity is then given by $I_{\text{SHG}}^{\text{total}} \propto |\pm \mathbf{P}_z^{\text{NF}}(2\omega) + \mathbf{P}_z^{\text{FF}}(2\omega)e^{i\phi_{\text{FF}}}|^2$ and reveals opposite (\pm) ferroelectric domains as regions of distinct brightness. Figures 3(a) and 3(b) corroborate the feasibility of the far field as reference field. It varies only slowly on a length scale of several microns. The strong modulation in Fig. 3(a) shows that near- and far-field contributions have comparable amplitude.

The following model can be used to assign the location of the domain walls and demonstrate the robustness and spatial resolution of our near-field experiment. The second-order polarization as source of the SHG near-field can be described by a homogeneous and discrete dipole distribution at the surface aligned in the $+z$ and $-z$ directions as shown sche-

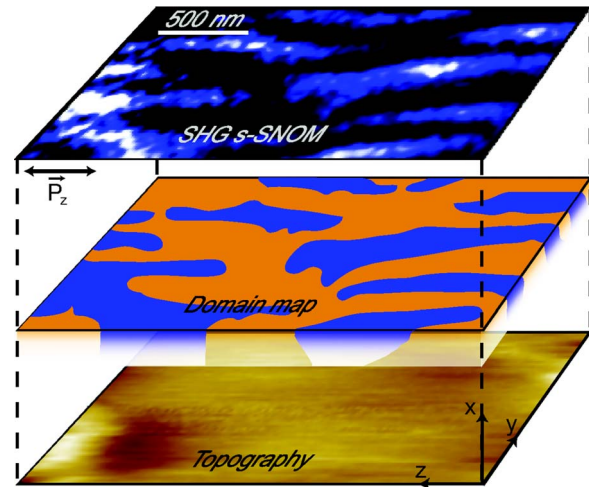


FIG. 4. (Color online) Ferroelectric domain topology of YMnO_3 . Near-field SHG imaging of the 180° domains in YMnO_3 , together with two-color map of the domain structure derived from the data using the discrete dipole model.

matically in Fig. 3(c). Using the dyadic free-space Green's function approach to solve the inhomogeneous Helmholtz equation with a $\delta(x)$ -function source term in the yz plane, the resulting field distribution above the surface can be derived numerically.^{35–37} Due to the translational invariance in the z direction, the solution is evaluated in the xy plane only. Considering 1-nm-spaced point dipoles and treating the tip as a point probe Fig. 3(d) show the derived overall spatial signal intensity modulation for four domains. As can be seen with increasing tip-sample distance the signal variation across the domain boundary blurs laterally since for large tip-sample distances the relative weight of the dipole density away from the boundary increases. The large tip-sample distance is also associated with an overall decrease in the evanescent SHG intensity, thus decreasing the signal contrast for a given reference intensity. For a tip apex radius of 20 nm and a typical tip-sample distance of ~ 10 nm this reveals a domain-wall-related change in signal from 10% to 90% across a distance of 50 nm in excellent agreement with the experimentally observed spatial variation in Fig. 2.

This model is then used to derive the distribution of domains from the maxima and minima of the SHG s -SNOM data together with the underlying spatially slowly varying far-field signal as illustrated for the signal cross section shown in Fig. 3(d). In the same way, the two-dimensional (2D) distribution of domains is derived by a 2D fit of the entire data set.

Figure 4 shows the resulting domain map together with the set of raw SHG s -SNOM data and the simultaneously acquired topographic scan. The two distinct regions represent the corresponding antiparallel domains. According to Fig. 3(b) the procedure is very robust even against large variations in tip-sample distance. As a result the position of the domain walls can be estimated to be accurate within ± 20 nm. However, due to the tip-evanescent field extending a few tens of nanometers, the subsurface continuation of the domain topology can slightly affect the domain assignment. Note that the wall thickness itself, expected to be only a few

unit cells wide,³⁸ is beyond the resolution of the experiment.

With domain sizes on the order of $\sim 1000 \times 200$ nm² corresponding to aspect ratios of $\sim 5:1$, the domains are anisotropically elongated along the hexagonal crystallographic z axis. While this reflects the uniaxial crystal structure and associated electrostatic anisotropy, the domain topology observed is highly irregular, unlike the straight lamellae type observed in classical ferroelectrics.^{9,28} Together with recent similar observations, e.g., on thin films of BiFeO₃,^{39,40} the different ferroelectric domain topologies observed might suggest a possibly distinct microscopic mechanisms responsible for ferroelectricity in magnetoelectric multiferroics.

The optical imaging of the nanoscopic domains in YMnO₃ has been enabled by taking advantage of the phase and symmetry sensitivities of SHG, the polarization-selective tip scattering, and the ultrahigh spatial resolution provided by s -SNOM. The self-homodyne phase-sensitive detection of a specific $\chi^{(2)}$ tensor component that reflects the ferroelectric symmetry parameter allows for probing even 180° domains, otherwise difficult by conventional techniques. While the approach is complementary to piezoelectric force microscopy

(PFM) or transmission electron microscopy (TEM) techniques for ferroelectric domain imaging,⁴¹ no external voltage needs to be applied and the intrinsic sample electrical conductivity does not affect the measurements. Demonstrated here for uniaxial YMnO₃, SHG s -SNOM is applicable also for multiaxial symmetries. As a purely nonlinear optical technique being sensitive to symmetry, it is applicable to the study of domain structure in any material with broken centrosymmetry associated with any form of ferroic order and provides spectral information. This will permit the noninvasive probing of electric and magnetic orders and their coexistence by just one technique. SHG s -SNOM can thus contribute to the yet incomplete understanding of the origin of magnetoelectric coupling in single-phase multiferroics, including local coupling effects arising in the distribution of nanoscopic domains and domain walls.^{6,42,43}

Funding from the National Science Foundation (NSF Career CHE-0748226), the EU-STREP MaCoMuFi, and the Deutsche Forschungsgemeinschaft (SPP 1133), and support from Thomas Elsaesser are greatly acknowledged.

- ¹J. Scott, *Ferroelectric Memories* (Springer, Berlin, 2000).
- ²R. C. Miller, *Phys. Rev.* **134**, A1313 (1964).
- ³M. Fejer, G. Magel, D. Jundt, and R. Byer, *IEEE J. Quantum Electron.* **28**, 2631 (1992).
- ⁴D. Polla and L. Francis, *Annu. Rev. Mater. Sci.* **28**, 563 (1998).
- ⁵T. Kimura, *Annu. Rev. Mater. Res.* **37**, 387 (2007).
- ⁶C. Thiele, K. Dörr, O. Bilani, J. Rödel, and L. Schultz, *Phys. Rev. B* **75**, 054408 (2007).
- ⁷D. Sa, R. Valenti, and C. Gros, *Eur. Phys. J. B* **14**, 301 (2000).
- ⁸G. Dolino, *Appl. Phys. Lett.* **22**, 123 (1973).
- ⁹Y. Uesu, S. Kurimura, and Y. Yamamoto, *Appl. Phys. Lett.* **66**, 2165 (1995).
- ¹⁰M. Flörshheimer, R. Paschotta, U. Kubitschek, C. Brillert, D. Hofmann, L. Heuer, G. Schreiber, C. Verbeek, W. Sohler, and H. Fuchs, *Appl. Phys. B: Lasers Opt.* **67**, 593 (1998).
- ¹¹I. Smolyaninov, A. Zayats, and C. Davis, *Opt. Lett.* **22**, 1592 (1997).
- ¹²S. Bozhevolnyi, K. Pedersen, T. Skettrup, X. Zhang, and M. Belmonte, *Opt. Commun.* **152**, 221 (1998).
- ¹³I. I. Smolyaninov, C. H. Lee, and C. C. Davis, *J. Microsc.* **194**, 426 (1999).
- ¹⁴W. Dickson, S. Takahashi, C. Morros, R. M. Bowman, J. M. Gregg, and A. V. Zayats, *Phys. Rev. B* **72**, 094110 (2005).
- ¹⁵W. Dickson, S. Takahashi, R. Pollard, and A. V. Zayats, *Appl. Phys. Lett.* **85**, 6341 (2004).
- ¹⁶L. Novotny, D. W. Pohl, and P. Regli, *J. Opt. Soc. Am. A Opt. Image Sci. Vis.* **11**, 1768 (1994).
- ¹⁷N. Bloembergen, *Nonlinear Optics* (Benjamin, New York, 1977).
- ¹⁸J. Levy, C. Hubert, and A. Trivelli, *J. Chem. Phys.* **112**, 7848 (2000).
- ¹⁹H. Ma and J. Levy, *Nano Lett.* **6**, 341 (2006).
- ²⁰L. Mahieu-Williams, S. Gresillon, M. Cuniot-Ponsard, and C. Boccara, *J. Appl. Phys.* **101**, 083111 (2007).
- ²¹C. C. Neacsu, J. Dreyer, N. Behr, and M. B. Raschke, *Phys. Rev. B* **73**, 193406 (2006).
- ²²R. E. Cohen and H. Krakauer, *Ferroelectrics* **136**, 65 (1992).
- ²³N. A. Hill, *J. Phys. Chem. B* **104**, 6694 (2000).
- ²⁴C. J. Fennie and K. M. Rabe, *Phys. Rev. B* **72**, 100103(R) (2005).
- ²⁵G. Nenert, M. Pollet, S. Marinell, G. R. Blake, A. Meetsma, and T. T. M. Palstra, *J. Phys.: Condens. Matter* **19**, 466212 (2007).
- ²⁶B. B. Van Aken, T. T. Palstra, A. Filippetti, and N. A. Spaldin, *Nature Mater.* **3**, 164 (2004).
- ²⁷N. Fujimura, T. Ishida, T. Yoshimura, and T. Ito, *Appl. Phys. Lett.* **69**, 1011 (1996).
- ²⁸S. Kurimura and Y. Uesu, *J. Appl. Phys.* **81**, 369 (1997).
- ²⁹M. Fiebig, T. Lottermoser, D. Froehlich, and S. Kallenbach, *Opt. Lett.* **29**, 41 (2004).
- ³⁰F. Lissalde and J. Peuzin, *Ferroelectrics* **4**, 159 (1972).
- ³¹C. Degenhardt, M. Fiebig, D. Fröhlich, T. Lottermoser, and R. V. Pisarev, *Appl. Phys. B: Lasers Opt.* **73**, 139 (2001).
- ³²C. Neacsu, G. Steudle, and M. Raschke, *Appl. Phys. B: Lasers Opt.* **80**, 295 (2005).
- ³³C. C. Neacsu, G. A. Reider, and M. B. Raschke, *Phys. Rev. B* **71**, 201402(R) (2005).
- ³⁴M. Fiebig, D. Fröhlich, T. Lottermoser, and M. Maat, *Phys. Rev. B* **66**, 144102 (2002).
- ³⁵M. Xiao, S. Bozhevolnyi, and O. Keller, *Appl. Phys. A: Mater. Sci. Process.* **62**, 115 (1996).
- ³⁶C. Tai, *Dyadic Green's Functions in Electromagnetic Theory* (Intext, 1971).
- ³⁷M. Xiao, *J. Mod. Opt.* **44**, 327 (1997).
- ³⁸J. Padilla, W. Zhong, and D. Vanderbilt, *Phys. Rev. B* **53**, R5969 (1996).
- ³⁹G. Catalan, H. Bea, S. Fusil, M. Bibes, P. Paruch, A. Barthelemy, and J. F. Scott, *Phys. Rev. Lett.* **100**, 027602 (2008).
- ⁴⁰Y. H. Chu *et al.*, *Appl. Phys. Lett.* **90**, 252906 (2007).
- ⁴¹Y.-H. Chu *et al.*, *Adv. Mater. (Weinheim, Ger.)* **18**, 2307 (2006).
- ⁴²W. Eerenstein, M. Wiora, J. L. Prieto, J. F. Scott, and N. D. Mathur, *Nature Mater.* **6**, 348 (2007).
- ⁴³R. Ramesh and N. A. Spaldin, *Nature Mater.* **6**, 21 (2007).